small structures
www.small-structures.com

Bonding Heterogeneity and Nanoprecipitation on Substituting the Anionic Framework in Mg_3Sb_2 for p-Type Zintl Thermoelectrics

*Nagendra Singh Chauhan and Takao Mori**

Designing zintl compounds with complex crystal structures and large unit cells containing heavy elements may inherit bonding heterogeneity-induced lattice anharmonicity, leading to intrinsically low thermal conductivity. In this work, alloying-induced bonding heterogeneity in the extensively explored α-$Mg_3(Sb, Bi)_2$ phase due to local atomic ordering, site preferences, and prevailing heterogenous interfaces is evaluated in the p-type $Mg_3(Sb_{1-2x}Bi_xSn_x)_2$-based polyanionic nanocomposites for different alloying concentrations. The inherent susceptibility for partial phase transition (trigonal → monoclinic) is observed upon alloying, which is driven by alterations in bonding patterns, localized distortion, and secondary phase formation. At low alloying content ($x \leq 0.05$), a trigonal (Sb, Sn) phase is observed, while for higher alloying content ($x \geq 0.1$), a cubic Mg_2Sn nanophase emerges. A synergistic reduction in thermal conductivity and enhanced power factor maximize the $zT \approx 0.25(\pm 0.05)$ at 673 K in the optimized p-type $Mg_3(Sb_{0.9}Bi_{0.025}Sn_{0.025})_2$ nanocomposites. The study highlights bonding heterogeneity-induced structural transitions as an inherent challenge, where the dominant role of anionic sites becomes pivotal for determining/deriving favorable structural and functional properties in $Mg_3(Sb, Bi)_2$-based zintl compounds.

1. Introduction

Low-grade waste heat recovery by thermoelectrics (TE) has garnered renewed attention in recent years, due to the outstanding n-type performance obtained in $Mg_3(Sb, Bi)_2$ solid solutions.[1–6] To complement this exceptional performance at the device level, ongoing efforts are aimed toward developing their low-cost and high-performance p-type counterpart, besides further optimization of their n-type TE figure of merit (zT) near room temperature.[7–9] Intrinsically, undoped Mg_3Sb_2 compound exhibits p-type conduction with a low hole concentration (n) $\approx 10^{17}$ cm^{-3} and a multivalley ($N_v \approx 6$) conduction band behavior near the Fermi level.[10,11] Upon heavy Bi alloying (≈25 at%) and subsequent doping by ≈1 at% with chalcogen group elements (i.e., Te, Se, S), a higher $n \approx 10^{19}$ cm^{-3} for n-type conduction was attained, leading to maximization of zT values ranging between 1.5 and 2 at ≈723 K for the optimized compositions.[1–4] Such high zT is comparable to, and even surpasses, many state-of-the-art n-type TE materials, leading to an impressive device performance with a conversion efficiency ($\eta \geq 7\%$) under a 300 K temperature difference (ΔT).[12,13] Thus, the anionic framework constituting a covalently bonded network formed by complex anions or metalloids plays a vital role in sustaining the "electron–crystal" electronic structure in doped Mg_3Sb_2 crystals, which also exhibit an inherently low lattice thermal conductivity (κ_L) ≈1 Wm^{-1} K^{-1} near room temperature.[14–17]

As a prominent and widely explored zintl phase, Mg_3Sb_2 is part of the broader family of zintl antimonides, which encompasses diverse crystal structures and compositions, though only a small subset has been investigated for their TE properties.[18] On crystal structure basis, $Mg_3(Sb, Bi)_2$ and its mixed-anion derivatives are classified as 1–2–2 zintl family that exhibits $CaAl_2Si_2$-type structure (Space Group: $P\bar{3}m1$, 164)[18–22] with an asymmetric unit cell having complicated bonds. Interestingly, Mg atoms reside in both the octahedrally coordinated interlayer Mg(I) site (i.e., the cation site) and the tetrahedrally coordinated intralayer Mg(II) site (i.e., within the anionic $[Mg_2Sb_2]^{2-}$ framework). The chemical bonding analysis of α-Mg_3Sb_2 indicates coordination flexibility of Mg—Sb bonds having both ionic and covalent character, wherein covalent bonding in the $[Mg_2Sb_2]^{2-}$ anionic framework enables high carrier mobility, while the ionic Mg^{2+} cations offer better dopability for carrier concentration optimization.[10,11] The site preference and occupancy patterns during the alloying/doping indicate that Mg(I) sites tend to be preferentially occupied by highly electropositive

N. S. Chauhan, T. Mori
Research Center for Materials Nanoarchitectonics (MANA)
National Institute for Materials Science (NIMS)
Namiki 1-1, Tsukuba 305-0044, Japan
E-mail: mori.takao@nims.go.jp

T. Mori
Graduate School of Pure and Applied Sciences
University of Tsukuba
1-1-1 Tennodai, Tsukuba, Ibaraki 305-8573, Japan

The ORCID identification number(s) for the author(s) of this article can be found under https://doi.org/10.1002/sstr.202400632.

DOI: 10.1002/sstr.202400632

alkaline earth metals and lanthanides (such as Ca, Sr, Ba, La, and Yb), while Mg(II) sites exhibit a higher affinity for alloying with more electronegative metals like Zn, Mn, and Cd.[21]

Among its anionic solid solutions, $Mg_3Sb_{2-x}Bi_x$ and its derivatives exhibit an excellent bandgap tunability which has allowed optimization of n-type properties by reducing the bandgap to enable efficient doping efficiency with Te/Se/S as dopants.[1–4] However, for p-type conduction, anionic doping strategies (i.e., substituting dopants on the Sb/Bi sites) in $Mg_3(Sb, Bi)_2$ and its related solid solutions have remained largely ineffective,[23–26] primarily due to its weak valence band degeneracy ($N_v = 1$).[27] Nevertheless, codoping approaches (Zn, Na, Yb, Ag, and/or Cu)[28–32] primarily targeting the cationic Mg(I) and/or anionic Mg(II) sites have remained effective in regulating and optimizing holes concentration, reaching an optimal $n \approx 10^{19}\,cm^{-3}$ to attain a maximum $zT \approx 0.8$ at around 773 K.[28–33] From a practical perspective, enhancing the TE performance of p-type $Mg_3(Sb, Bi)_2$ to match its n-type counterpart still remains critical and an ongoing challenge for realization of the α-Mg_3Sb_2-based device, with a maximum conversion efficiency (η) ≈5.5% at the hot-side temperature of 573 K, reported till date.[34]

Complex multinary zintl compounds constituting a polyanionic (ternary, quaternary, and higher) framework can offer new basis for deriving novel functionalities and understanding of the poor dopability of p-type $Mg_3(Sb, Bi)_2$. We report $Mg_3(Sb_{1-2x}Bi_xSn_x)_2$-based polyanionic nanocomposites with bonding heterogeneity-induced locally distorted structures and nanoprecipitation, synthesized employing ball milling and spark plasma sintering. The preferences for specific site occupancies of (Bi, Sn) substitutions in Mg_3Sb_2 were assessed employing a (3 + 1) dimensional superspace approach, which provided critical insights into the atomic-scale interactions and local atomic ordering in the constituting α-Mg_3Sb_2 phase. Partial phase transition (trigonal → monoclinic), nanoprecipitation of trigonal (Sb, Sn, Bi) phase for low alloying content $x \approx 0.05$, and Mg_2Sn nanoprecipitation for increasing alloying content $x > 0.05$, was observed implying locally distorted structures. The present study highlights the inherent susceptibility of $Mg_3(Sb, Bi)_2$-based polyanionic solid solutions for bonding heterogeneity, structural transitions, and secondary phase formations and their implications on thermal and electrical transport properties. It also demonstrates how alloying strategies require vital consideration of structural and bonding modifications to effectively attain better dopability and targeted functionalization of transport properties of zintl compounds.

2. Results and Discussion

2.1. Phase Compositions, Phase Segregation, and Hierarchical Microstructure

The powder diffraction X-ray diffraction (PXRD) patterns of representative $Mg_3(Sb_{1-2x}Bi_xSn_x)_2$ nanocomposite samples are shown in **Figure 1**a, which indicate major peaks corresponding to trigonal α-Mg_3Sb_2 phase (Space Group : $P\bar{3}m1$, 164) in all the alloyed compositions. For low alloying content $x \approx 0.05$, additional peaks corresponding to the trigonal (Sb, Sn, Bi) phase (Space Group: $R\bar{3}m$, 166) were also indexed and indicated by star (*), while for higher alloying content $x \geq 0.1$, peaks corresponding to cubic Mg_2Sn phase (Space Group: $Fm\bar{3}m$, 225), as indicated by inverted triangle (▼), appear, implying α-Mg_3Sb_2 phase instability and secondary phase precipitation process during synthesis. With increasing equiatomic (Sn, Bi) content, that is, x, the major and overlapping (101) and (011) PXRD peaks shift to lower angles (Figure 1b) when compared with synthesized $Mg_3Sb_{1.9}Sn_{0.1}$, suggesting an expansion of the α-Mg_3Sb_2 lattice. In addition to lattice expansion, shifts in major overlapping peaks can be attributed to secondary-phase formation, potentially altering the Sb/Bi ratio in the synthesized nanocomposites. Beyond $x \geq 0.2$, additional peaks corresponding to tetragonal Sn phase (Space Group: *I41/amd* 141) indicated by an empty inverted triangle (▽) were also observed. Samples with higher alloying content are also more chemically stable, during unavoidable exposure to atmospheric conditions during XRD measurements, as indicated by absence of MgO impurity peaks, which is distinctively observed for $x \approx 0.05$ and indicated by filled circles. The presence of extra peaks corresponding to secondary phases even in synthesized $Mg_3Sb_{1.9}Sn_{0.1}$ is indicative of the discordant nature of Sn/Sb atoms in Mg—Sb—Sn-based compositions, wherein secondary-phase precipitation was also observed.[35–37] Notably, the synthesized $Mg_3(Sb_{1-2x}Bi_xSn_x)_2$ compositions lie well within the solid solubility limits of Bi (i.e., $x \approx 0.4$)[23] for $Mg_3Sb_{2-x}Bi_x$ and agree well with the previous structural observations reported for $Mg_3Sb_{2-x}Sn_x$ polycrystals.[36]

To understand phase stability, potential phase transformations, and optimal compositions in the synthesized $Mg_3(Sb_{1-2x}Bi_xSn_x)_2$ nanocomposites, ternary phase diagram of Mg—Sb—Sn at room temperature (an isothermal section)[35] is overlaid over the evaluated modified Gibbs free energy of mixing and is shown in Figure 1c. Previous investigation has revealed the observed difficulty in synthesizing ternary Mg—Sb—Sn compounds,[35–38] wherein binary α-Mg_3Sb_2 compound was evaluated[35] to coexist with Mg_2Sn, Sn, and SnSb in phase equilibria. The Gibbs free energy of mixing (ΔG_m) landscape influences the extent of solid solution formation, where the lowest ΔG_m implies thermodynamic stability, in regions corresponding to the synthesized compositions. The secondary-electron scanning electron microscopy images presented in Figure 1d display backscattered electron (BSE) micrograph of characteristic fracture surface morphology i a representative sample, indicative of transgranular fracture. This fracture mode is characterized by crack propagation occurring through the grains rather than along grain boundaries. The fracture surfaces reveal prominent cleavage facets with aligned lamellae patterns, which are characteristic of plastic deformation within individual grains. The nanoprecipitation promotes local ordering, contributing to the development of layered structures that accommodate anionic substructures. Consequently, the material's response to stress likely involves both grain-level plasticity and substructural adjustments, leading to the observed layered morphology.[39]

The presence of nanoinclusions within the microstructure can be attributed to localized compositional variations caused by the discordant Sn atoms, which nucleate and segregate from the supersaturated $Mg_3(Sb, Bi)_2$ solid solution as indicated by elemental mapping shown in Figure 1e. The energy-dispersive

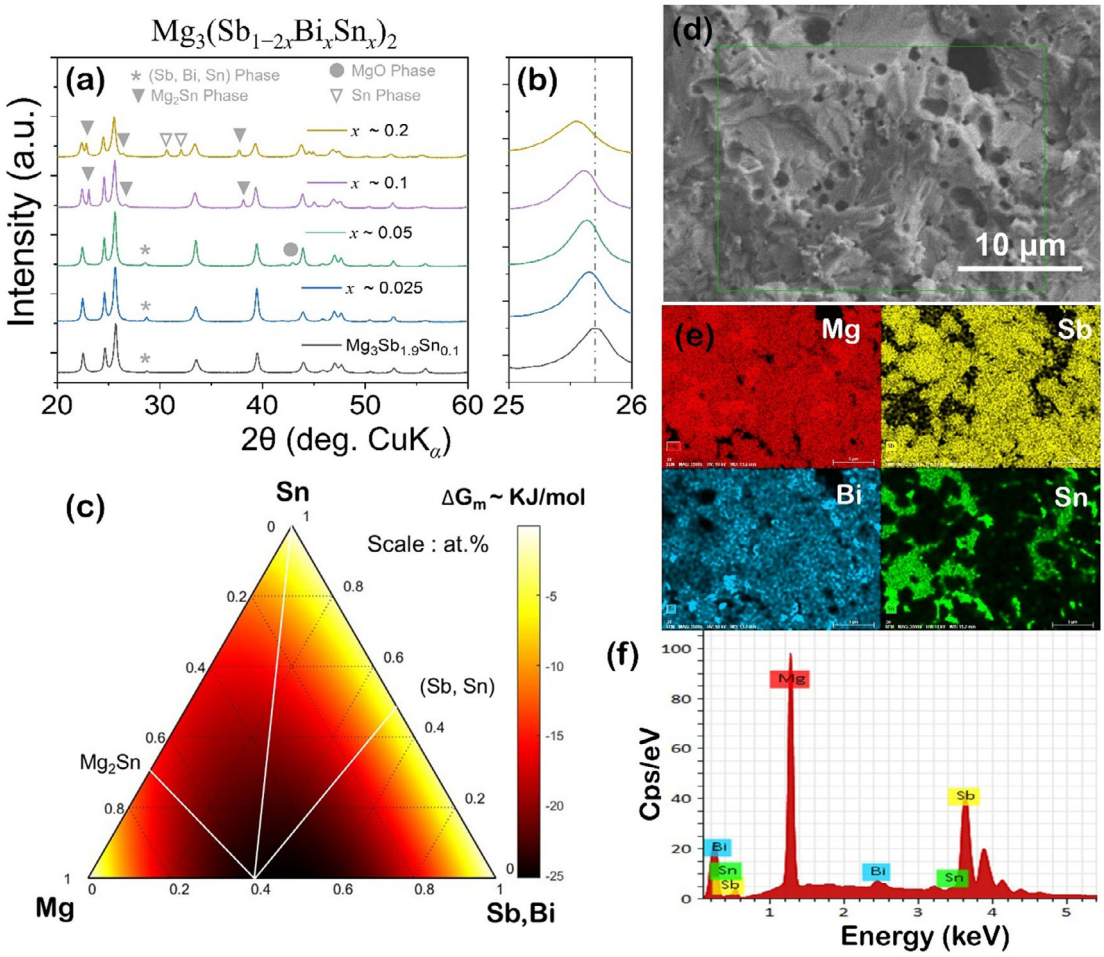

Figure 1. a) PXRD diffraction of synthesized $Mg_3(Sb_{1-2x}Bi_xSn_x)_2$ polycrystals. Magnified view indicating shift in b) major 101 and 011 peaks of α-Mg_3Sb_2. c) Isothermal section at 573 K of Mg—Sn—(Sb, Bi) phase diagram and triangulation of modified Gibbs free energy indicating low ΔG_m region for the synthesized compositions. d) Fractured BSE micrograph for with $x \approx 0.2$, indicating transgranular fracture and embedded nanoprecipitation of (Sn, Sb) phase and Mg_2Sn, distinctively identifiable in e) elemental mapping and f) EDX spectrum showing elemental peaks.

X-ray (EDX) spectrum shown in Figure 1f, confirms the existence of an extended solid solution comprising Mg_2Sn, Bi, and SnSb within the Mg_3Sb_2 matrix, agreeing well with the previously reported phase equilibria studies in the Mg—Sb—Sn system.[35] Thus, a complex interplay between the different phases in the heterogeneous microstructure with nanoscale features of the synthesized nanocomposites is indicative of the structural differences between Mg_2Sn and Mg_3Sb_2 phases that preclude the formation of a complete solid solution agreeing well with previous observations.[37,38]

2.2. Structural Parameters and Monoclinic Phase Transitions

Substitutions at the anionic framework in zintl phases are highly susceptible to causing structural distortions, which may result in lowering of symmetry, changes in bonding patterns, and formation of monoclinic variants.[18,21,22,40] These distortions are often driven by electronic factors or size differences between substituted atoms.[26] In the synthesized $Mg_3(Sb_{1-2x}Bi_xSn_x)_2$ nanocomposites, an extensive structural disorder with a partial loss of trigonal symmetry leading to monoclinic phase transitions (Space Group: *C2/m*, 12) was also indexed during refinement, implying a locally distorted configuration and chemical disordering in the synthesized polycrystals. It is noteworthy that the observance of monoclinic structure in the synthesized polycrystals as a highly distorted variant owes structural similarity to the high-pressure monoclinic structure for Mg_3Sb_2 and Mg_3Bi_2 reported previously at critical transition at above 7.8 and 4.0 GPa, respectively.[41] However, the synthesized polycrystals exhibit an irreversible and co-existing monoclinic phase as shown in **Figure 2**a, in contrast to the pressure-induced displacive and reversible (trigonal ↔ monoclinic) phase transition, reported previously.[41] The refinements of the PXRD evaluates the monoclinic *C2/m* unit cell (formula unit = 6) with a volume per formula unit of ≈500 Å^3.

The refined lattice parameter of the α-Mg_3Sb_2 phases, as shown in Figure 2b, obtained by Le Bail refinement, reveals an initial decrease in lattice parameters *a* and *c* for lower alloying content, followed by a consistent increase with higher alloying

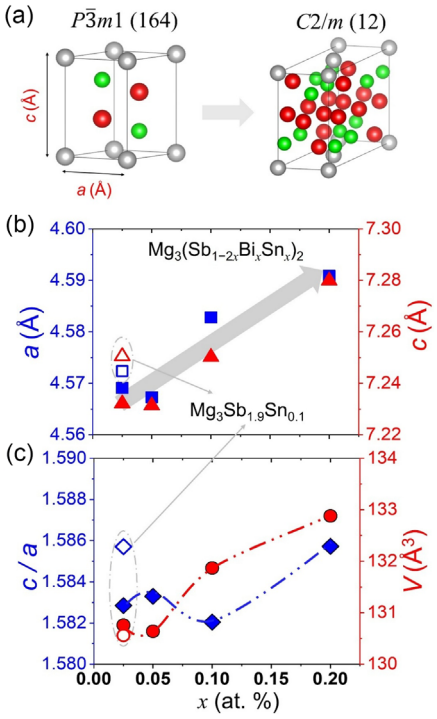

Figure 2. a) Unit cells of α-$Mg_3(Sb, Bi)_2$ and its partially transformed monoclinic phase, with Mg(I) in gray, Mg(II) in red, and (Sb, Bi) in green. b) Refined lattice parameters *a* (square) and *c*(triangle), along with c). *c*/*a* ratio (diamond) and volume (circle) for unit cell of major α-$Mg_3(Sb, Bi)_2$ phase in $Mg_3(Sb_{1-2x}Bi_xSn_x)_2$ nanocomposites. Corresponding structural parameters for synthesized $Mg_3Sb_{1.9}Sn_{0.1}$, shown with empty symbols.

levels. The refined XRD patterns are shown in Figure S1–S3, Supporting Information, which displays the observed, calculated, and difference profiles along with the Bragg peaks of the constituting phases and refinement parameters are tabulated in **Table 1**. The Sn, Bi dissolution into the Mg_3Sb_2 matrix, particularly of Bi atoms within the α-Mg_3Sb_2 phase, implies accordance with Vegard's Law. However, even for low alloying content, that is, $x \leq 0.05$, complex coordination and trigonal (Sb, Sn, Bi) phase precipitation may result in α-Mg_3Sb_2 phase lattice contraction. For the higher alloyed compositions, that is, $x \geq 0.1$, cubic Mg_2Sn phase precipitation and larger elemental volume of Bi in comparison to Sb atoms led to larger and increasing lattice parameter *a* and *c*, implying dopant solubility in the constituting phases. When Sn is introduced at Sb site, it occupies specific anionic sites (causing Sb atoms precipitation), leading to alterations in the local lattice environment and symmetry of α-Mg_3Sb_2 phase. Thus, the average crystal structure of the synthesized $Mg_3(Sb_{1-2x}Bi_xSn_x)_2$ polycrystals and stability of constituting phases are related to the amount of dopant, besides the differences in the atomic size and electronegativity of the host and substituted Sb anions. It is worth mentioning that the presence of excess Mg at cationic sites can stabilize or destabilize certain phases, potentially promoting or preventing the monoclinic phase transitions. In contrast to the anisotropic structural collapse with relative compression of the *a* and *c*-axes,[41] the monoclinic phase formation is accompanied by unit cell expansion of α-Mg_3Sb_2 unit cell. The alloying content dependence of the *c*/*a* ratio and unit cell volume of the major trigonal α-Mg_3Sb_2 phase, as shown in Figure 2c, reveals a more elongated unit cell for higher alloying content, with varying *c*/*a* ratio. When compared to doped $Mg_3Sb_{1.9}Sn_{0.1}$, codoping Sn and Bi atoms causes a reduction in the *c*-axis length relative to the *a*-axis, which can be ascribed to instability and partial loss of symmetry of major α-Mg_3Sb_2 phase. As the volume increase is significant, it is indicative of dopant solubility and a growing potential for precipitation of secondary phases at higher alloying contents, discussed subsequently. The partial loss of trigonal symmetry in the synthesized $Mg_3(Sb_{1-2x}Bi_xSn_x)_2$ by phase transition occurs at the anionic $[Mg_2Sb_2]^{2-}$ framework and can be ascribed to the discordant Sn atoms, preferentially occupying specific lattice sites in the alloyed polycrystal. The expanding unit cell volume for trigonal phase is indicative of a displacive phase transition wherein the distorted coordination polyhedral within the anionic framework may constitute bonding heterogeneity.

2.3. Bonding Heterogeneity and Low Thermal Conductivity

Mixed-anion compounds, which contain polyanions as separate building blocks, may result in locally distorted structures where more than one anion bonds to a cation. The bonding environment in Mg defect complex, particularly the coordination and geometric arrangement of Mg and Sb atoms, contributes to its overall stability or functionality. In the synthesized $Mg_3(Sb_{1-2x}Bi_xSn_x)_2$ nanocomposites, the formation of $MgSb_6$ octahedra and $MgSb_4$ tetrahedra as well as their interactions through shared corners and edges to prevailing nanoclusters was understood by evaluating bond lengths and occupancies in the trigonal α-Mg_3Sb_2 phase, a polar intermetallic phase. The Mg(I)—Mg(II) distances in Mg_3Sb_2 are ≈3.736 Å, while the Mg—Sb distances range from about 2.8 to 3.2 Å.[11] Particularly, Mg(I)—Sb is slightly longer than Mg(II)—Sb, suggesting that both Mg—Mg and Mg—Sb interactions are significant in α-Mg_3Sb_2. The Mg(I) atoms are coordinated by six Sb atoms in a trigonal prismatic arrangement, while Mg(II) atoms are tetrahedrally coordinated by four Sb atoms as shown in **Figure 3**a. The bonding in Mg_3Sb_2 is predominantly ionic with some covalent character in the Mg—Sb interactions,[42] wherein the Mg(I)—Mg(II) interactions, while present, are relatively weaker than the Mg—Sb bonds.

To evaluate bonding heterogeneity, positional modulation of the atomic sites was introduced, after several refinement cycles, considering isotropic displacement parameters up to the fourth order of the Fourier terms A_n and B_n ($n = 1$–4) using both cosine and sine components. The anion 4*b* Wyckoff site is occupied by the Sb and Mg(II) atoms whereas the cation 4*a* Wyckoff site is occupied by Mg(I) atoms, as shown in Figure 3b. The presence of three anions (i.e., Sb, Sn, and Bi) at the 4*a* Wyckoff site in $(Mg_2Sb_{2-2x}Bi_xSn_x)^{2-}$ motifs may result in an enhanced degree of anionic disorder in the trigonal α-Mg_3Sb_2 phase leading to locally distorted configurations with partially broken symmetry. The altering bonding distances of octahedral Mg(I) and tetrahedral Mg(II) environments, ranging from 2.87 to 3.02 Å, for lower ($x \leq 0.05$) and higher ($x \geq 0.1$) substitution, suggest compressibility and expansion, respectively. Softer and longer

Table 1. Constituting phases in synthesized $Mg_3(Sb_{1-2x}Bi_xSn_x)_2$ nanocomposites.

Composition[a]	Space group	Lattice parameters	Volume	R-factors[b]		
				GOF	R_p	R_{wp}
$Mg_3Sb_{1.9}Sn_{0.1}$	$P\bar{3}m1$	$a=b=4.5724(1)$, $c=7.2505(2)$, $\alpha=\beta=90°$, $\gamma=120°$	130.56(1)	1.59	3.76	5.12
	$C2/m$	$a=14.493(1)$, $b=4.396(1)$, $c=7.908(1)$, $\alpha=\gamma=90°$; $\beta=90.858(3)$	503.74(1)			
	$R\bar{3}m$	$a=b=4.303(1)$, $c=11.335(1)$, $\alpha=\beta=90°$, $\gamma=120°$	181.80(1)			
$x\approx0.025$	$P\bar{3}m1$	$a=b=4.5691(1)$, $c=7.2322(2)$, $\alpha=\beta=90°$, $\gamma=120°$	130.76(1)	1.63	3.65	5.05
	$C2/m$	$a=14.413(1)$, $b=4.348(1)$, $c=7.873(1)$, $\alpha=\gamma=90°$; $\beta=90.907(6)$	493.38(1)			
	$R\bar{3}m$	$a=b=4.299(1)$, $c=11.300(3)$, $\alpha=\beta=90°$, $\gamma=120°$	180.92(1)			
$x\approx0.05$	$P\bar{3}m1$	$a=b=4.5673(1)$, $c=7.2314(1)$, $\alpha=\beta=90°$, $\gamma=120°$	130.64(1)	1.55	3.38	4.80
	$C2/m$	$a=14.452(1)$, $b=4.340(1)$, $c=7.866(1)$, $\alpha=\gamma=90°$; $\beta=91.013(5)$	493.35(1)			
	$R\bar{3}m$	$a=b=4.317(1)$, $c=11.307(2)$, $\alpha=\beta=90°$, $\gamma=120°$	182.51(1)			
$x\approx0.1$	$P\bar{3}m1$	$a=b=4.5828(1)$, $c=7.2502(2)$, $\alpha=\beta=90°$, $\gamma=120°$	131.87(1)	1.72	4.02	5.30
	$C2/m$	$a=14.517(1)$, $b=4.463(1)$, $c=7.935(1)$, $\alpha=\gamma=90°$; $\beta=90.606(6)$	503.74(1)			
	$Fm\bar{3}m$	$a=b=c=6.6795(2)$, $\alpha=\beta=\gamma=90°$	298.01(1)			
$x\approx0.2$	$P\bar{3}m1$	$a=b=4.5909(1)$, $c=7.2799(3)$, $\alpha=\beta=90°$, $\gamma=120°$	132.88(1)	1.34	3.00	3.91
	$C2/m$	$a=14.581(1)$, $b=4.496(1)$, $c=7.998(1)$, $\alpha=\gamma=90°$; $\beta=90.847(5)$	524.29(2)			
	$Fm\bar{3}m$	$a=b=c=6.7477(2)$, $\alpha=\beta=\gamma=90°$	307.24(1)			
	$I41/amd$	$a=b=5.8287(2)$, $c=3.1798(2)$, $\alpha=\beta=\gamma=90°$	108.03(1)			

[a]Space group, lattice parameters, unit cell volume (Å^2), and refinement parameters (weighted profile (R_{wp}); profile (R_p); and expected (R_{exp}) *R*-factor). Standard deviations are given in parentheses. [b]$R_{wp}=\sqrt{\frac{\sum w_i(y_i^{obs}-y_i^{calc})^2}{\sum w_i(y_i^{obs})^2}}$; $R_p=\frac{\sum|y_i^{obs}-y_i^{calc}|}{\sum y_i^{obs}}$; $GOF=\frac{R_{wp}}{R_{exp}}$.

Mg(I)—(Sb, Bi, Sn) bonds reveal an initial decrease and subsequent increase in bond length, corroborating well with the decreasing and increasing lattice parameter *c*, respectively. Remarkably, a similar trend for the shorter Mg(II)—(Sb, Bi, Sn) bonds constituting the polyanionic framework was evaluated, wherein an altering bonding patterns was also evaluated for higher ($x\geq0.1$) substitution in the synthesized $Mg_3(Sb_{1-2x}Bi_xSn_x)_2$ nanocomposites. Interestingly, atomic displacement evaluated for trigonal α-Mg_3Sb_2 and shown in Figure S7, Supporting Information, indicates a significant variation for Mg(II) and Sb atoms constituting the anionic framework for varying alloying content. Thus, synthesized $Mg_3(Sb_{1-2x}Bi_xSn_x)_2$ constituting polyanionic framework is bound to have bonding heterogeneity-induced localized distortion and secondary phase formation with altered bonding lengths. A comprehensive understanding of bonding heterogeneity and structural transitions requires integrating advanced techniques such as atom probe tomography,[43–45] nuclear magnetic resonance,[43] X-ray photoelectron spectroscopy,[46] high-resolution transmission electron microscopy,[45–48] and Raman spectroscopy,[46,47] which should be the focus of future research to explore local atomic and electronic environments. Moreover, interfacial lattice matching analysis[49] can be used in conjunction with crystal orbital Hamilton population evaluations[50] to study the compatibility and interactions between different phases at their interfaces.

The constituting locally distorted structures with a diverse bonding environment in mixed-anion $Mg_3(Sb_{1-2x}Bi_xSn_x)_2$-based nanocomposites are anticipated to result in significant variations in interatomic force constants, splitting of phonon frequencies, and enhanced anharmonicity when compared to single-anion Mg_3Sb_2.[51] The locally distorted structures resulting from altered coordination numbers (CN) in mixed-anion materials introduce bonding heterogeneity, which effectively contributes to achieving low κ_L as indicated in Figure 3c. The Sn atoms preferentially occupy lattice sites with distorted square prismatic coordination (CN ≈ 8, *Fm-3m*), distinct from the monocapped trigonal prismatic sites (CN ≈ 7, *P-3m1*) typically occupied by the substituted host Sb atoms in the anionic framework, leading to bond heterogeneity. Moreover, higher dopant solubility at the polyanionic framework enhances scattering of phonons by mass/strain fluctuations particularly for lower substitution.

Despite Sn limited solubility, a pronounced phonon scattering was attained, thus lowering the κ_L to >30% in comparison to Bi-[23] and Sn-doped Mg_3Sb_2 counterparts in the measured temperature range. In $Mg_3(Sb_{1-2x}Bi_xSn_x)_2$-based nanocomposites, κ_L decreases from $\approx1.35\,Wm^{-1}K^{-1}$ ($Mg_3Sb_{1.9}Sn_{0.1}$) to $\approx0.9\,Wm^{-1}K^{-1}$ ($x=0.05$) at 298 K, implying enhanced scattering of lower-frequency phonons. The limited dopant solubility and coexisting secondary phases in the synthesized $Mg_3(Sb_{1-2x}Bi_xSn_x)_2$ nanocomposites have contrasting effects on κ_L: wherein heterogeneous interfaces (presumably Mg_3Sb_2—Mg_2Sn)[37,38] instead of enhancing phonon scattering apparently decrease interfacial thermal resistance, resulting in higher κ_L. Furthermore, higher κ_L is evaluated for higher alloying content $x\approx0.2$, where undesirable (Sn/SnSb) phases evolve, violating the T^{-1} temperature-dependent κ_L more drastically, thereby compensating the phonon scattering occurring at heterogeneous interfaces.[17] Thus, thermal transport indicates critical role of

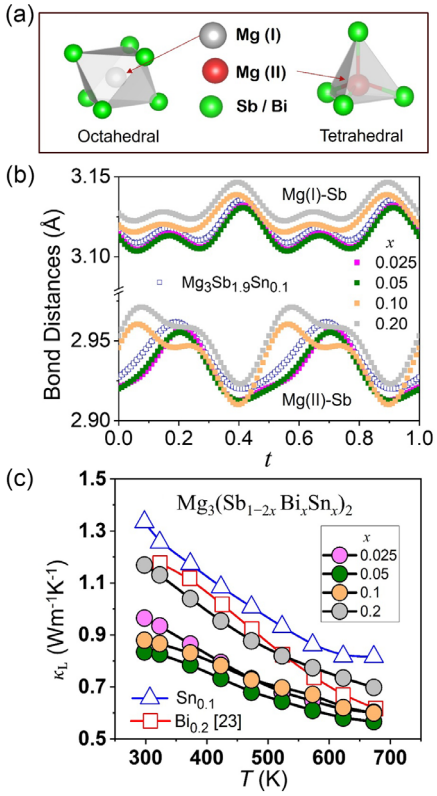

Figure 3. a) Schematic showing two nonequivalent Mg sites with tetrahedral and octahedral polyhedra and b) evaluated bond distances for Mg(I)—Sb and Mg(II)—Sb atoms, in trigonal α-$Mg_3(Sb, Bi)_2$ phase. c) Temperature-dependent lattice thermal conductivity (κ_L) of the synthesized $Mg_3(Sb_{1-2x}Bi_xSn_x)_2$ nanocomposites shown along with previously reported[23] values of $Mg_3Sb_{1.8}Bi_{0.2}$ polycrystals.

structural inhomogeneity, bonding heterogeneity, and phase separation in increasing the lattice anharmonicity, which is effective in reducing κ_L of the synthesized $Mg_3(Sb_{1-2x}Bi_xSn_x)_2$ nanocomposites.

2.4. Electronic Band Structure, Ionized Impurity Scattering Mechanism, and *zT* Enhancement

The $Mg_3(Sb, Bi)_2$-based zintl compounds exhibit a complex band structure with a challenging large and asymmetric unit cell.[11,52] Similar to state-of-the-art $(Sb, Bi)_2Te_3$ alloys, electronic band structure of $Mg_3(Sb, Bi)_2$ constitutes low-symmetry conduction band minimum (CBM) with high band degeneracy ($N_v \approx 6$). However, low band degeneracy (i.e., $N_v \approx 1$) of valence band maximum (VBM) limits the optimization of power factor for p-type conduction.[27] Notably, transitioning from semiconductor-to-metallic behavior occurs on varying the Sb content $Mg_3Sb_{2-x}Bi_x$ with minimum κ measured for $x \approx 0.5$.[14] To simulate and analyze the effects of disorder on the electronic band structure of the synthesized $Mg_3(Sb_{1-2x}Bi_xSn_x)_2$ nanocomposites, Korringa-Kohn-Rostoker (KKR) -coherent potential approximation (CPA) approach is employed which replaces the actual disordered crystal structure with an effective medium Green's function and a self-energy.[53–55] Even at low doping levels, the KKR-CPA approach provides a realistic representation of the disordered doped system without necessitating large supercells,[56–59] making it particularly relevant for our evaluation of (Sn, Bi) codoped Mg_3Sb_2. The electronic band structure with estimated spectral weight variations corresponding to Bloch spectral functions (BSFs) in arbitrary units (a.u.) of $Mg_3Sb_{1.9}Sn_{0.1}$ and $Mg_3Sb_{1.8}Sn_{0.1}Bi_{0.1}$ is shown in **Figure 4**a,b, respectively.

The band dispersion shows notable changes upon Sn doping, with the VBM at the Γ point and the CBM at the K point, agreeing well with the evaluation made previously employing supercell approach.[36] Since the VBM and CBM are located at different points in k-space (Γ and K, respectively) with coinciding energies, the resulting zero indirect bandgap allows carriers to undergo transition from the valence to the conduction band without a change in momentum, but via an intermediate state. Diffused spectral weight and overlapping bands at the Γ and A points in the valence band suggest that electronic states are spread over a range of energies implying disorder, impurities, or strong electron–electron interactions. The upward shift of the VBM points to an enhanced p-type conductivity, indicating metallic or semimetallic behaviour due to the zero indirect bandgap and band overlap. Previous calculations have also suggested the VBM of Mg_3Sb_2 at the Brillouin zone center (Γ) being dominated by the p orbitals of Sb anions that are composed of in-plane $p_{x,y}$ and out-of-plane p_z orbital.[2,36,60] Furthermore, the reduction in $\sigma(T)$ upon Bi codoping could be well associated with a pronounced chemical disorder which enhances carrier scattering in the $(Mg_2Sb_{2-2x}Bi_xSn_x)^{2-}$ motifs. The negative bandgap, accompanied by an upward shift of the valence bands, indicates enhanced interactions between electronic states, while an increased orbital overlap may spatially confine electrons, reducing the density of free charge carriers in the system.

To understand carrier characteristics, Hall measurement results at room temperature are shown in Figure 4c. The $Mg_3(Sb_{1-2x}Bi_xSn_x)_2$ nanocomposites for $x \approx 0.025$ reveal a significant increase in both carrier mobility (μ_H) and carrier concentration (n_H), in comparison to synthesized $Mg_3Sb_{1.9}Sn_{0.1}$, which can be ascribed primarily to the upshift of VBM. However, with increasing substitution, decreasing n_H and deteriorating μ_H were measured, attributed to an enhanced carrier scattering. The effects of Sn and Bi substitutions on temperature-dependent electrical transport behavior of the synthesized $Mg_3Sb_{1.9}Sn_{0.1}$ and $Mg_3(Sb_{1-2x}Bi_xSn_x)_2$ nanocomposites are shown in Figure 4d–f, alongside the previously reported $Mg_3Sb_{1.8}Bi_{0.2}$ for comparison.[23] The temperature-dependent Seebeck coefficient $S(T)$, shown in Figure 4d, implies p-type conduction, as also corroborated from the Hall measurement data. At room temperature, S for $Mg_3Sb_{1.9}Sn_{0.1}$ ($\approx$143 μV K^{-1}) increases linearly with temperature, reaching a value of $\approx$253 μV K^{-1} at 673 K. As the cosubstitution of Sn and Bi increases, the Seebeck coefficient at room temperature shows a marginal decrease for $x \approx 0.25$, likely due to changes in the carrier concentration or scattering mechanisms. However, for phase-separated sample $x \approx 0.1$ having heterogeneous interfaces (presumably Mg_3Sb_2—Mg_2Sn), S increases to $\approx$227 μV K^{-1} at 300 K and decreases thereafter, which can be ascribed primarily to carrier filtering.

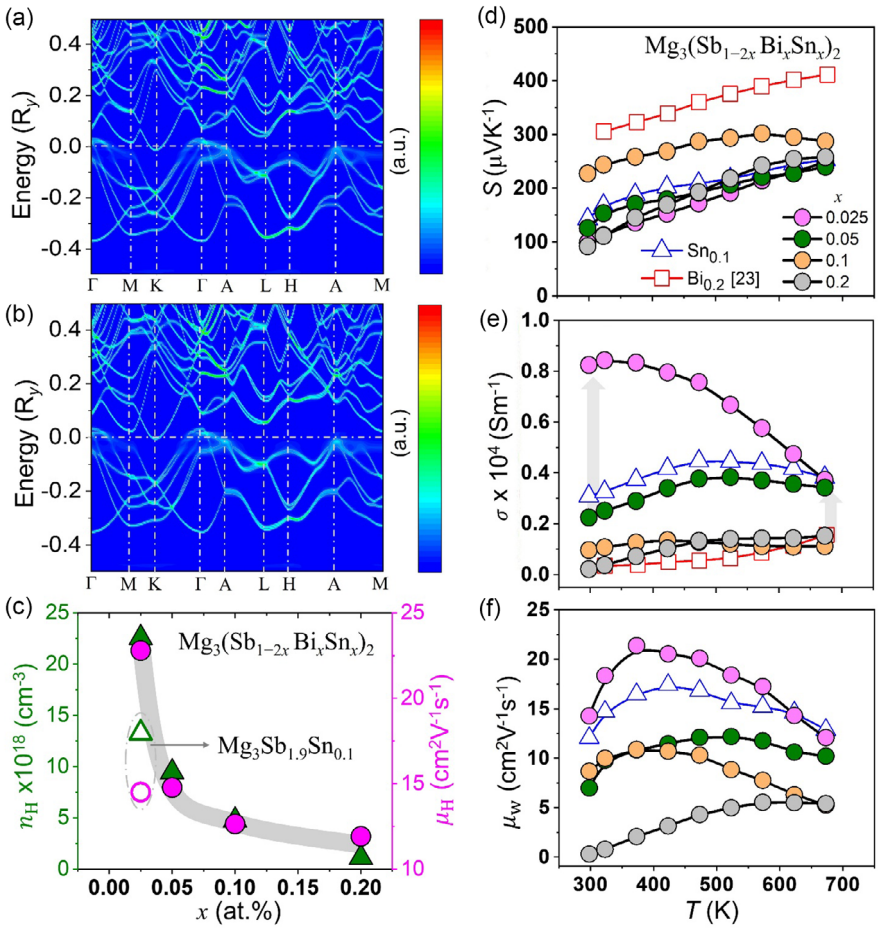

Figure 4. Calculated electronic band structure of a) $Mg_3Sb_{1.9}Sn_{0.1}$ and b) $Mg_3Sb_{1.8}Sn_{0.1}Bi_{0.1}$. Normalized scale reflects the BSFs in arbitrary units. c) Hall carrier concentration and mobility at 300 K. Temperature-dependent d) Seebeck coefficient, e) electrical conductivity, and f) weighted mobility of $Mg_3(Sb_{1-2x}Bi_xSn_x)_2$ nanocomposites shown along with previously reported[23] values of $Mg_3Sb_{1.8}Bi_{0.2}$ polycrystals.

The temperature-dependent electrical conductivity $\sigma(T)$ within the temperature range of 300–673 K shown in Figure 4e indicates a significant increase in $\sigma(T)$ for $x \approx 0.25$ to a measured value of $\approx 8.2 \times 10^3$ S m^{-1} at room temperature, corresponding to ≈1.6-fold enhancement over $Mg_3Sb_{1.9}Sn_{0.1}$ ($\approx 3.1 \times 10^3$ S m^{-1}), which agrees well with the values reported previously.[36] This increase is primarily due to the introduction of additional charge carriers by Sn substitution. However, with (Sn, Bi) cosubstitution, $\sigma(T)$ decreases as a result of additional scattering centers (reducing carrier mobility), primarily due to increasing phase fractions of secondary phases, which reduce carrier mobility. Additionally, modifications in the band structure by Bi substitution are likely contribute to this decline in electrical conductivity, as observed previously in $Mg_3Sb_{1-x}Bi_x$.[23] The $\sigma(T)$ of phase-separated nanocomposites at higher alloying content aligns with the $\sigma(T)$ of $Mg_3Sb_{1-x}Sn_x$ reported previously and implies the detrimental effects of phase separation on electrical conductivity.[36] This suggests that the presence of segregated phases leads to increased scattering and reduced μ_H ultimately compromising the electrical transport for higher substitutions.

The weighted mobility (μ_w)[61] derived $S(T)$ and $\sigma(T)$ measurements, that closely mirror μ_H, are also shown in Figure 4f as it reflects electron mobility weighted by the density of electronic states, providing insights into the electronic structure and scattering mechanisms. The observed increase in μ_w with temperature suggests ionized impurity scattering as the primary mechanism of carrier scattering. At lower temperatures, slower carriers allow more interactions with charged impurities, while as temperature rises, carriers move faster, reducing scattering from ionized impurities and thus increasing μ_w. However, at higher temperatures, mobility typically decreases due to increased lattice vibrations (phonon scattering), indicating the coexistence of multiple scattering mechanisms, each varying in influence with temperature and alloying content.

The temperature-dependent thermal conductivity $\kappa(T)$ shown in **Figure 5**a also indicates significant reduction in $Mg_3(Sb_{1-2x}Bi_xSn_x)_2$ nanocomposites, in comparison to Bi-[23] and Sn-doped Mg_3Sb_2 counterparts ascribed primarily to lattice anharmonicity, phase separation, and dynamic structural disorder. $\kappa(T)$ is significantly lowered even for low alloying content as shown in Figure 5b, when compared to $Mg_3Sb_{1.9}Sn_{0.1}$ both at low (≈300 K) and high (≈673 K) temperature. The increase in κ_L for $x > 0.05$ can be attributed to the higher κ of the Mg_2Sn phase[62] and Sn segregation, which presumably enhances the phonon

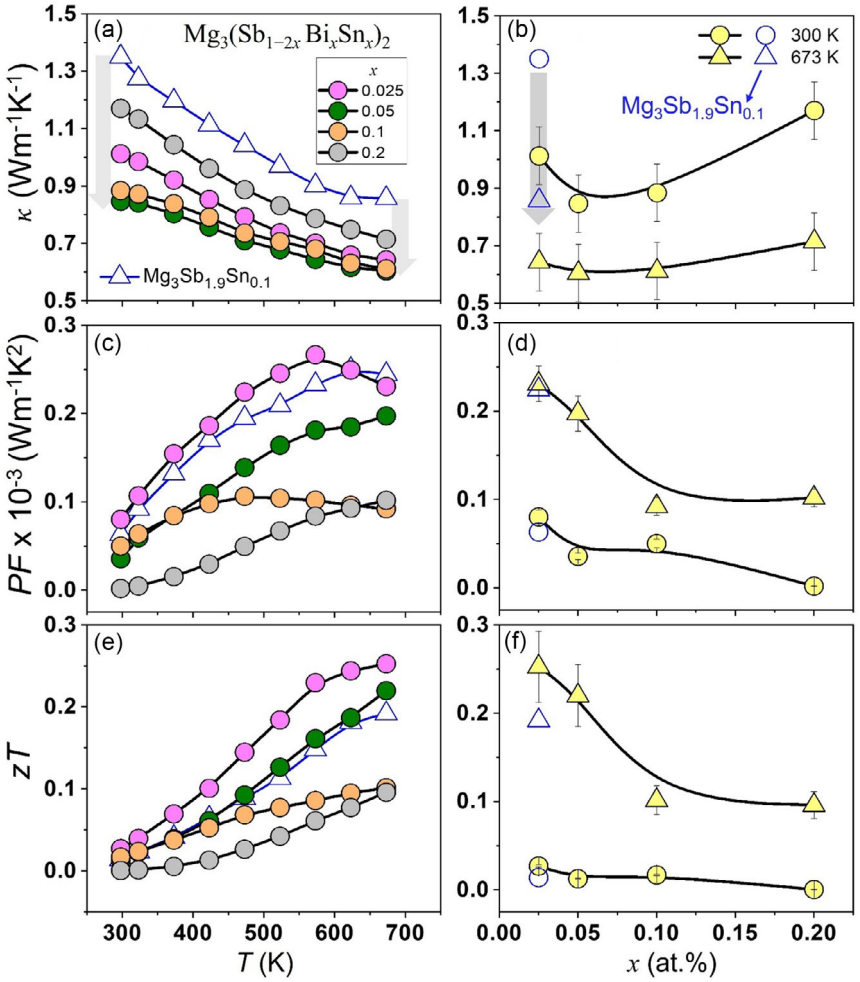

Figure 5. Temperature dependence and alloying content dependence of a,b) total thermal conductivity, c,d) power factor, and e,f) TE figure of merit (zT) of nominal $Mg_3(Sb_{1-2x}Bi_xSn_x)_2$ nanocomposites. Corresponding TE transport parameters for synthesized $Mg_3Sb_{1.9}Sn_{0.1}$, shown with empty symbols.

propagation by creating additional thermally conductive pathways. The power factor (Figure 5c,d) shows a marginal deterioration compared to $Mg_3Sb_{1.9}Sn_{0.1}$ for low alloying content ($x \leq 0.05$) and decreases significantly thereafter with increasing alloying content, primarily to reduction in both $S(T)$ and $\sigma(T)$ due to secondary phase formations. However, the enhancement is more significant in relation to $Mg_3Sb_{1.8}Bi_{0.2}$,[23] for lower temperatures (<600 K), achieving a maximum power factor of $\approx$2.5 μW cm^{-1} K^{-2} at 573 K, thus, implying that the cosubstitution of Sn and Bi sustains the power factor for low alloying content ($x \leq 0.05$) and remains detrimental for increasing substitution ($x \geq 0.1$) due to Mg_2Sn phase precipitation. The zT shown in Figure 5e for all the synthesized $Mg_3(Sb_{1-2x}Bi_xSn_x)_2$ nanocomposites increases with temperature, wherein $Mg_3Sb_{1.9}Sn_{0.1}$ exhibits significantly higher $zT \approx 0.2$ ($\pm$ 0.05), which increases marginally for $x \approx 0.25$–0.5 (as shown in Figure 5f), primarily due to a notable κ reduction, thus, demonstrating that (Sn, Bi) substitutions effectively improve the zT, but inherent distortion and phase separation prove detrimental to further enhance the zT, which optimizes only for lower content ($x \leq 0.05$) in synthesized $Mg_3(Sb_{1-2x}Bi_xSn_x)_2$ nanocomposites.

Thus, a limited understanding of structural changes that occur during doping or alloying hinders insights into their prominent effects on conduction/valence bands and defect chemistry. While challenges such as limited solubility and poor doping efficiency persist, improving carrier mobility and power factor in p-type Mg_3Sb_2 necessitates exploring codoping or alloying, especially within the anionic framework along with effective cationic dopants such as Na, Yb, Ag, Zn, and/or Cu.[28–32] Thus, complex multinary p-type $Mg_3(Sb,Bi)_2$-based zintl nanocomposites, with polyanionic frameworks, offer potential for realizing all-Mg_3Sb_2-based TE devices with enhanced TE conversion efficiency. However, addressing intrinsic monoclinic phase transition, nanoprecipitation susceptibility, and bonding heterogeneity remains critical for optimizing transport properties.

3. Conclusion

Anionic solid solutions constituting a polyanionic substructure can offer a versatile approach to favorably tune p-type conduction in $Mg_3(Sb, Bi)_2$ by regulating the composition of the anionic

framework. The synthesized (Sn, Bi) cosubstituted Mg_3Sb_2-based polyanionic solid solutions exhibit bonding heterogeneity in dominant α-$Mg_3(Sb, Bi)_2$ phase, intrinsic partial monoclinic phase transitions, and nanoprecipitation susceptibility with varying alloying content. Coexistence of different crystal structures and phases relays poor dopability and limited solubility, highlighting the critical role of anionic framework for phase stability. Despite low content ($x \leq 0.05$), structural changes induced by (Sn, Bi) substitution reduce κ and synergistically enhance carrier mobility and concentrations, leading to improved power factor and zT. Phase separation of cubic Mg_2Sn for higher alloying content ($x \geq 0.1$) enhances κ_L and deteriorates carrier transport, thereby drastically reducing the zT. Thus, alloying/substitution strategies must carefully account for structural and bonding modifications to enhance dopability and tailor the transport properties of zintl compounds.

Supporting Information

Supporting Information is available from the Wiley Online Library or from the author.

Acknowledgements

This research was supported by JST Mirai Program, Japan (grant no. JPMJMI19A1).

Conflict of Interest

The authors declare no conflict of interest.

Author Contributions

Nagendra Singh Chauhan: conceptualization (equal); formal analysis (lead); investigation: (lead); methodology (lead); writing—original draft (lead). **Takao Mori**: conceptualization (equal); funding acquisition (lead); project administration (lead); resources (lead); supervision (lead); writing—review and editing (lead).

Data Availability Statement

The data that support the findings of this study are available from the corresponding author upon reasonable request.

Keywords

bonding heterogeneities, nanocomposites, phase separations, thermoelectrics, zintl

Received: December 2, 2024
Revised: February 13, 2025
Published online: March 5, 2025

[1] H. Tamaki, H. K. Sato, T. Kanno, *Adv. Mater.* **2016**, *28*, 10182.
[2] J. Zhang, L. Song, S. H. Pedersen, H. Yin, L. T. Hung, B. B. Iversen, *Nat. Commun.* **2017**, *8*, 13901.
[3] J. Zhang, L. Song, A. Mamakhel, M. R. V. Jørgensen, B. B. Iversen, *Chem. Mater.* **2017**, *29*, 5371.
[4] J. Zhang, L. Song, K. A. Borup, M. R. V. Jørgensen, B. B. Iversen, *Adv. Energy Mater.* **2018**, *8*, 1702776.
[5] S. Bano, R. Chetty, J. Babu, T. Mori, *Device* **2024**, *2*, 100408.
[6] J. Mao, H. Zhu, Z. Ding, Z. Liu, G. A. Gamage, G. Chen, Z. Ren, *Science* **2019**, *365*, 495.
[7] L. Wang, N. Sato, Y. Peng, R. Chetty, N. Kawamoto, D. H. Nguyen, T. Mori, *Adv. Energy Mater.* **2023**, *13*, 2301667.
[8] L. Wang, W. Zhang, S. Y. Back, N. Kawamoto, D. H. Nguyen, T. Mori, *Nat. Commun.* **2024**, *15*, 6800.
[9] H. Cho, S. Y. Back, N. Sato, Z. Liu, W. Gao, L. Wang, H. D. Nguyen, N. Kawamoto, T. Mori, *Adv. Funct. Mater.* **2024**, *34*, 2407017.
[10] H. Shang, Z. Liang, C. Xu, J. Mao, H. Gu, F. Ding, Z. Ren, *Research* **2020**, *2020*, 1219461.
[11] A. Li, C. Fu, X. Zhao, T. Zhu, *Research* **2020**, *2020*, 1934848.
[12] Z. Liu, N. Sato, W. Gao, K. Yubuta, N. Kawamoto, M. Mitome, K. Kurashima, Y. Owada, K. Nagase, C.-H. Lee, J. Yi, K. Tsuchiya, T. Mori, *Joule* **2021**, *5*, 1196.
[13] Y. Sun, Y. Zhu, H. Wu, N. Qu, L. Xie, J. Zhu, Z. Liu, Q. Zhang, W. Cai, F. Guo, J. Sui, *Energy Environ. Sci.* **2024**, *17*, 738.
[14] K. Imasato, M. Wood, S. Anand, J. J. Kuo, G. J. Snyder, *Adv. Energy Sustainability Res.* **2022**, *3*, 2100208.
[15] T. Kanno, H. Tamaki, M. Yoshiya, H. Uchiyama, S. Maki, M. Takata, Y. Miyazaki, *Adv. Funct. Mater.* **2021**, *31*, 2008469.
[16] J. Hu, J. Zhu, X. Dong, M. Guo, Y. Sun, W. Shi, Y. Zhu, H. Wu, F. Guo, Y. Zhang, Z. Ge, Q. Zhang, Z. Liu, W. Cai, J. Sui, *Small* **2023**, *19*, 2301382.
[17] Y. Zhu, Y. Xia, Y. Wang, Y. Sheng, J. Yang, C. Fu, A. Li, T. Zhu, J. Luo, C. Wolverton, G. J. Snyder, J. Liu, W. Zhang, *Research* **2020**, *2020*, 4589786.
[18] N. Kazem, S. M. Kauzlarich, *Handbook on the Physics and Chemistry of Rare Earths*, Elsevier, Amsterdam **2016**, pp. 177–208.
[19] M. Martinez-Ripoll, A. Haase, G. Brauer, *Acta Crystallogr. B* **1974**, *30*, 2006.
[20] C. Zheng, R. Hoffmann, R. Nesper, H. G. Von Schnering, *J. Am. Chem. Soc.* **1986**, *108*, 1876.
[21] J. Wang, J. Mark, K. E. Woo, J. Voyles, K. Kovnir, *Chem. Mater.* **2019**, *31*, 8286.
[22] S. M. Kauzlarich, K. P. Devlin, C. J. Perez, *Thermoelectric Energy Conversion*, Elsevier, Amsterdam **2021**, pp. 157–182.
[23] A. Bhardwaj, N. S. Chauhan, D. Misra, *J. Mater. Chem. A* **2015**, *3*, 10777.
[24] A. Bhardwaj, D. Misra, *RSC Adv.* **2014**, *4*, 34552.
[25] J. Tani, H. Ishikawa, *Phys. B* **2020**, *588*, 412173.
[26] N. S. Chauhan, T. Mori, *J. Mater. Chem. A* **2024**, *12*, 32703.
[27] P. Gorai, B. R. Ortiz, E. S. Toberer, V. Stevanović, *J. Mater. Chem. A* **2018**, *6*, 13806.
[28] L. Huang, T. Liu, X. Mo, G. Yuan, R. Wang, H. Liu, X. Lei, Q. Zhang, Z. Ren, *Mater. Today Phys.* **2021**, *21*, 100564.
[29] Z. Ren, J. Shuai, J. Mao, Q. Zhu, S. Song, Y. Ni, S. Chen, *Acta Mater.* **2018**, *143*, 265.
[30] M. Tiadi, V. Trivedi, S. Kumar, P. K. Jain, S. K. Yadav, R. Gopalan, D. K. Satapathy, M. Battabyal, *ACS Appl. Mater. Interfaces* **2023**, *15*, 20175.
[31] V. P. Kannan, V. Lourdhusamy, I. Paulraj, S. Madanagurusamy, C.-J. Liu, *ACS Appl. Mater. Interfaces* **2024**, *16*, 58677.
[32] M. Tiadi, M. Battabyal, P. Jain, A. Chauhan, D. K. Satapathy, R. Gopalan, *Sustainable Energy Fuels* **2021**, *5*, 4104.
[33] A. Bhardwaj, N. S. Chauhan, S. Goel, V. Singh, J. Pulikkotil, T. Senguttuvan, D. Misra, *Phys. Chem. Chem. Phys.* **2016**, *18*, 6191.
[34] Z. Liang, C. Xu, S. Song, X. Shi, W. Ren, Z. Ren, *Adv. Funct. Mater.* **2023**, *33*, 2210016.

[35] J. Zhang, J. Wang, Y. Yuan, *Calphad* **2021**, *75*, 102361.
[36] Y. Wang, X. Zhang, Y. Liu, Y. Wang, J. Zhang, M. Yue, *Vacuum* **2020**, *177*, 109388.
[37] E. Dong, Y. Zhu, S. Tan, W. Liu, J. Wang, W. Zhang, *Acta Mater.* **2022**, *236*, 118139.
[38] Y. Zhu, R. Shu, F. Jiang, A. Elsukova, P. O. Å. Persson, P. Eklund, W. Liu, *ACS Appl. Nano Mater.* **2023**, *6*, 6133.
[39] P. Zhao, W. Xue, Y. Zhang, S. Zhi, X. Ma, J. Qiu, T. Zhang, S. Ye, H. Mu, J. Cheng, X. Wang, S. Hou, L. Zhao, G. Xie, F. Cao, X. Liu, J. Mao, Y. Fu, Y. Wang, Q. Zhang, *Nature* **2024**, *631*, 777.
[40] S. Baranets, A. Ovchinnikov, S. Bobev, *Handbook on the Physics and Chemistry of Rare Earths*, Elsevier, Amsterdam **2021**, pp. 227–324.
[41] M. Calderón-Cueva, W. Peng, S. M. Clarke, J. Ding, B. L. Brugman, G. Levental, A. Balodhi, M. Rylko, O. Delaire, J. P. S. Walsh, S. M. Dorfman, A. Zevalkink, *Chem. Mater.* **2021**, *33*, 567.
[42] J. Zhang, L. Song, M. Sist, K. Tolborg, B. B. Iversen, *Nat. Commun.* **2018**, *9*, 4716.
[43] T. Luo, J. J. Kuo, K. J. Griffith, K. Imasato, O. Cojocaru-Mirédin, M. Wuttig, B. Gault, Y. Yu, G. J. Snyder, *Adv. Funct. Mater.* **2021**, *31*, 2100258.
[44] J. J. Kuo, Y. Yu, S. D. Kang, O. Cojocaru-Mirédin, M. Wuttig, G. J. Snyder, *Adv. Mater. Interfaces* **2019**, *6*, 1900429.
[45] R. Shu, Z. Han, A. Elsukova, Y. Zhu, P. Qin, F. Jiang, J. Lu, P. O. Persson, J. Palisaitis, A. Le Febvrier, *Adv. Sci.* **2022**, *9*, 2202594.
[46] M. Tiadi, S. Kumar, P. K. Jain, D. K. Satapathy, M. Battabyal, *ACS Appl. Mater. Interfaces* **2025**, *17*, 4996.
[47] M. Tiadi, D. K. Satapathy, M. Battabyal, *Phys. Rev. B* **2024**, *109*, 195201.
[48] P. Nan, A. Li, L. Cheng, K. Wu, Z. Liang, F. Lin, C. Fu, T. Zhu, B. Ge, *Mater. Today Phys.* **2021**, *21*, 100524.
[49] Q. Zhang, J. Li, N. S. Chauhan, L. Wang, Z. Huang, W. Fan, K. Hayashi, S. Chen, J. Fan, Y. Miyazaki, *J. Mater. Chem. A* **2023**, *11*, 18811.
[50] Q. Zhang, H. Li, N. S. Chauhan, L. Wang, W. Fan, S. Chen, J. Fan, Y. Miyazaki, *Mater. Today Energy* **2024**, *44*, 101656.
[51] N. Sato, N. Kuroda, S. Nakamura, Y. Katsura, I. Kanazawa, K. Kimura, T. Mori, *J. Mater. Chem. A* **2021**, *9*, 22660.
[52] Z. Li, P. Graziosi, N. Neophytou, *NPJ Comput. Mater.* **2024**, *10*, 8.
[53] H. Akai, P. Dederichs, *J. Phys. C: Solid State Phys.* **1985**, *18*, 2455.
[54] T. Kotani, H. Akai, *Phys. Rev. B* **1996**, *54*, 16502.
[55] H. Akai, M. Ogura, N. H. Long, *J. Phys.: Condens. Matter* **2009**, *21*, 064241.
[56] A. Gonis, G. Stocks, W. Butler, H. Winter, *Phys. Rev. B* **1984**, *29*, 555.
[57] N. S. Chauhan, Y. Miyazaki, *Mater. Adv.* **2022**, *3*, 8498.
[58] N. S. Chauhan, Y. Miyazaki, *J. Alloys Compd.* **2022**, *908*, 164623.
[59] S. Misra, B. Wiendlocha, S. El Oualid, A. Dauscher, B. Lenoir, C. Candolfi, *J. Mater. Chem. A* **2024**, *12*, 1166.
[60] W. Zhang, J.-F. Halet, T. Mori, *J. Mater. Chem. A* **2023**, *11*, 24228.
[61] G. J. Snyder, A. H. Snyder, M. Wood, R. Gurunathan, B. H. Snyder, C. Niu, *Adv. Mater.* **2020**, *32*, 2001537.
[62] L. Zhang, J. Li, H. Chen, J. Feng, R. Liu, *J. Mater. Chem. C* **2024**, *12*, 8935.